

New precise measurement of R_{uds} and R between 3.08 and 3.72 GeV at the KEDR detector

V.V. Anashin^a, O.V. Anchugov^a, V.M. Aulchenko^{a,b}, E.M. Baldin^{a,b}, G.N. Baranov^{a,c}, A.K. Barladyan^a, A.Yu. Barnyakov^{a,b}, M.Yu. Barnyakov^{a,b}, S.E. Baru^{a,b}, I.Yu. Basok^a, A.M. Batrakov^a, E.A. Bekhtenev^a, A.E. Blinov^{a,b}, V.E. Blinov^{a,b,c}, A.V. Bobrov^{a,b}, V.S. Bobrovnikov^{a,b}, A.V. Bogomyagkov^{a,b}, A.E. Bondar^{a,b}, A.R. Buzykaev^{a,b}, P.B. Cheblakov^{a,b}, V.L. Dorohov^{a,c}, S.I. Eidelman^{a,b}, D.N. Grigoriev^{a,b,c}, S.A. Glukhov^a, V.V. Kaminskiy^a, S.E. Karnaev^a, G.V. Karpov^a, S.V. Karpov^a, K.Yu. Karukina^{a,c}, D.P. Kashtankin^a, P.V. Kasyanenko^a, T.A. Kharlamova^a, V.A. Kiselev^a, V.V. Kolmogorov^a, S.A. Kononov^{a,b}, K.Yu. Kotov^a, A.A. Krasnov^a, E.A. Kravchenko^{a,b}, V.N. Kudryavtsev^{a,b}, V.F. Kulikov^{a,b}, G.Ya. Kurkin^{a,c}, I.A. Kuyanov^a, E.B. Levichev^{a,c}, D.A. Maksimov^{a,b}, V.M. Malyshev^a, A.L. Maslennikov^{a,b}, O.I. Meshkov^{a,b}, S.I. Mishnev^a, I.A. Morozov^a, I.I. Morozov^{a,b}, S.A. Nikitin^a, I.B. Nikolaev^{a,b}, I.N. Okunev^a, A.P. Onuchin^{a,b,c}, S.B. Oreshkin^a, A.A. Osipov^{a,b}, I.V. Ovtin^{a,c}, S.V. Peleganchuk^{a,b}, S.G. Pivovarov^{a,c}, P.A. Piminov^a, V.V. Petrov^a, V.G. Prisekin^{a,b}, O.L. Rezanova^{a,b}, A.A. Ruban^{a,b}, G.A. Savinov^a, A.G. Shamov^{a,b}, D.N. Shatilov^a, D.A. Shvedov^a, B.A. Shwartz^{a,b}, E.A. Simonov^a, S.V. Sinyatkin^a, A.N. Skrinsky^a, A.V. Sokolov^{a,b}, D.P. Sukhanov^a, A.M. Sukharev^{a,b}, E.V. Starostina^{a,b}, A.A. Talyshv^{a,b}, V.A. Tayursky^{a,b}, V.I. Telnov^{a,b}, Yu.A. Tikhonov^{a,b}, K.Yu. Todyshev^{a,b,*}, A.G. Tribendis^a, G.M. Tumaikin^a, Yu.V. Usov^a, A.I. Vorobiov^a, V.N. Zhilich^{a,b}, A.A. Zhukov^a, V.V. Zhulanov^{a,b}, A.N. Zhuravlev^{a,b}

^a*Budker Institute of Nuclear Physics, 11, akademika Lavrentieva prospect, Novosibirsk, 630090, Russia*

^b*Novosibirsk State University, 2, Pirogova street, Novosibirsk, 630090, Russia*

^c*Novosibirsk State Technical University, 20, Karl Marx prospect, Novosibirsk, 630092, Russia*

arXiv:1805.06235v2 [hep-ex] 28 Jun 2018

Abstract

The present work continues a series of the KEDR measurements of the R value that started in 2010 at the VEPP-4M e^+e^- collider. By combining new data with our previous results we measured the values of R_{uds} and R at nine center-of-mass energies between 3.08 and 3.72 GeV. The total accuracy is about or better than 2.6% at most of energy points with a systematic uncertainty of about 1.9%.

1. Introduction

The ratio of the radiatively corrected total cross section of electron-positron annihilation into hadrons to the lowest-order QED cross section of the muon pair production is referred to as the value of R . The R values are critical in various precision tests of the Standard Model, e.g. $R(s)$ measurements are employed to determine the anomalous magnetic moment of the muon $(g-2)_\mu$ and the value of the electromagnetic fine structure constant at the Z^0 peak $\alpha(M_Z^2)$ [1, 2], the running strong coupling constant $\alpha_s(s)$ and heavy quark masses [3].

More than ten experiments contributed to the $R(s)$ measurement in the energy range between the $p\bar{p}$ and $D\bar{D}$ thresholds [4, 5, 6, 7, 8, 9, 10, 11, 12, 13, 14, 15, 16]. The most accurate results were obtained in the experiments of BES-II [14] and KEDR [15, 16], in which the accuracy of about 3.3% was reached.

For the considered energy range, systematic uncertainties give a substantial contribution to the total accuracy of the $R(s)$ quantity. This fact motivated us to repeat the R measurement for the given energy range after repairing and upgrading the detector. In 2014 the region of the J/ψ and $\psi(2S)$ resonances was scanned in the KEDR experiment with an integrated luminosity of about 1.3 pb^{-1} .

2. VEPP-4M collider and KEDR detector

The e^+e^- collider VEPP-4M [17] is operated in the 2×2 bunches mode in the wide range of the beam energy. The working luminosity of VEPP-4M is about $10^{30} \text{ cm}^{-2}\text{s}^{-1}$ in the vicinity of the J/ψ resonance.

The beam energy in this experiment is determined using the resonant depolarization method (RDM) [18, 19] with the relative accuracy of about 10^{-6} . The results of RDM calibrations are interpolated to calculate the energy during data taking with an accuracy of about 10 keV [20, 21].

The KEDR detector and its performance are described in detail elsewhere [22]. The detector contains a vertex detector (VD), drift chamber (DC), time-of-flight (TOF) system of scintillation counters, particle identification system based on aerogel Cherenkov counters, electromagnetic calorimeter (liquid krypton in the barrel part and CsI crystals in the endcaps), superconducting solenoid and muon system inside the magnet yoke. The superconducting solenoid produces a magnetic field of 0.6 T. The detector has a tagging system of scattered electrons for studying two-photon processes. The on-line luminosity measurement is performed by two single bremsstrahlung monitors in the e^+ and e^- direction.

The trigger consists of two hardware levels: the primary (PT) and the secondary one (ST) [23]. The PT is based on

*. Corresponding author, e-mail: todyshev@inp.nsk.su

signals from the TOF counters and fast signals from the CsI and LKr calorimeters, whereas the ST uses optimally shaped calorimeter signals and the information from the VD, DC and TOF.

At the end of 2013, the repair and upgrade of the detector were completed. We replaced the vacuum chamber with a new wider one to reduce possible accelerator background. The preamplifiers of the VD were reconfigured and equipped with additional copper foil screens to suppress the crosstalk. The drift chamber was renovated and a few layers were repaired. A second layer of the aerogel Cherenkov counters was installed. The barrel part of the TOF system was equipped with additional magnetic screens to counteract the reduction of signal amplitudes in photomultipliers in the magnetic field. The entire krypton was cleaned of electronegative impurities.

3. Experiment

The purpose of the experiment was to repeat the R scan carried out by KEDR in 2011, in addition we collected data at the energy point below the J/ψ . The total hadronic cross section was measured at eight points between 3.08 and 3.72 GeV. The value of energy was calculated by interpolating the resonance depolarization results obtained in calibration runs.

The actual energies and the integrated luminosity at the points are presented in Table 1. To determine resonance parameters the additional data samples of about 0.34 pb^{-1} were taken in the vicinity of the J/ψ and $\psi(2S)$ resonances. A measurement of beam energy by the resonance depolarization method was carried out at least once at each listed point off the resonance peak regions. The assigned energy errors are due to the drift of the parameters of the accelerator during data taking. The data points and the resonance fits are shown in Fig. 1.

Table 1: Center-of-mass energy \sqrt{s} and integrated luminosity $\int \mathcal{L} dt$.

Point	\sqrt{s} , MeV	$\int \mathcal{L} dt$, nb $^{-1}$
1	3076.7 ± 0.2	$103.45 \pm 0.98 \pm 0.93$
2	3119.2 ± 0.2	$77.15 \pm 0.86 \pm 0.69$
3	3221.8 ± 0.2	$93.18 \pm 0.98 \pm 0.84$
4	3314.7 ± 0.4	$157.69 \pm 1.31 \pm 1.42$
5	3418.3 ± 0.8	$150.46 \pm 1.33 \pm 1.35$
6	3499.6 ± 1.1	$125.76 \pm 1.23 \pm 1.13$
7	3618.1 ± 0.4	$159.97 \pm 1.43 \pm 1.44$
8	3719.6 ± 0.2	$130.90 \pm 1.34 \pm 1.18$

4. Data analysis

4.1. Analysis procedure

The observed electron-positron hadronic annihilation cross section is determined as follows:

$$\sigma_{\text{obs}}(s) = \frac{N_{\text{mh}} - N_{\text{res.bg.}}}{\int \mathcal{L} dt}, \quad (1)$$

where N_{mh} is the number of events passing selection criteria, $N_{\text{res.bg.}}$ is the residual machine background which is discussed in Sec. 4.6 and $\int \mathcal{L} dt$ is the integrated luminosity.

For any observed cross section the R value is determined from

$$R = \frac{\sigma_{\text{obs}}(s) - \sum \varepsilon_{\text{bg}}(s) \sigma_{\text{bg}}(s) - \sum \varepsilon_{\psi}(s) \sigma_{\psi}(s)}{\varepsilon(s) (1 + \delta(s)) \sigma_{\mu\mu}^0(s)}, \quad (2)$$

where $\sigma_{\mu\mu}^0(s)$ is the Born cross section for $e^+e^- \rightarrow \mu^+\mu^-$ and $\varepsilon(s)$ is the detection efficiency for the single-photon annihilation to hadrons. The second term in the numerator corresponds to the physical background from lepton pair production and two-photon processes. The detection efficiencies ε and ε_{bg} were obtained from simulation.

The third term is a contribution of the J/ψ and $\psi(2S)$. Unlike Refs. [11, 12, 13, 14], we take into account narrow resonances explicitly instead of including them in the radiation correction $\delta(s)$. The narrow resonance cross section depends on the combination $\varepsilon_{\psi} \Gamma_{ee} \mathcal{B}_h$. The efficiencies ε_{ψ} were extracted by fitting the data at the resonance regions, thus the obtained resonance cross section is not sensitive to the world-average values of the leptonic width Γ_{ee} and the hadronic branching fraction \mathcal{B}_h used. Computations of a narrow resonance cross section, the resonance – continuum interference and the resonance fitting procedure are described in more detail in Refs. [21, 24].

The floating parameters were the detection efficiency ε_{ψ} at the world-average values of the leptonic width Γ_{ee} and its product by the hadronic branching fraction \mathcal{B}_h , the machine energy spread and the magnitude of the continuum cross section observed at the reference point below the resonance. The J/ψ and $\psi(2S)$ detection efficiencies, the collision energy spreads obtained and the χ^2 probabilities of the fits are presented in Table 2.

Table 2: Efficiency, energy spread and χ^2 probability of the fits of the J/ψ and $\psi(2S)$ resonances (statistical errors only are presented). The reference energy points for the energy spread parameters correspond to masses J/ψ and $\psi(2S)$ mesons taken from PDG [25].

	Efficiency, %	σ_w , MeV	$P(\chi^2)$, %
J/ψ	78.72 ± 0.89	0.785 ± 0.004	53.5
$\psi(2S)$	80.65 ± 1.95	1.262 ± 0.045	99.4

Table 3 lists the relative contribution of the J/ψ and $\psi(2S)$ to the observed cross section.

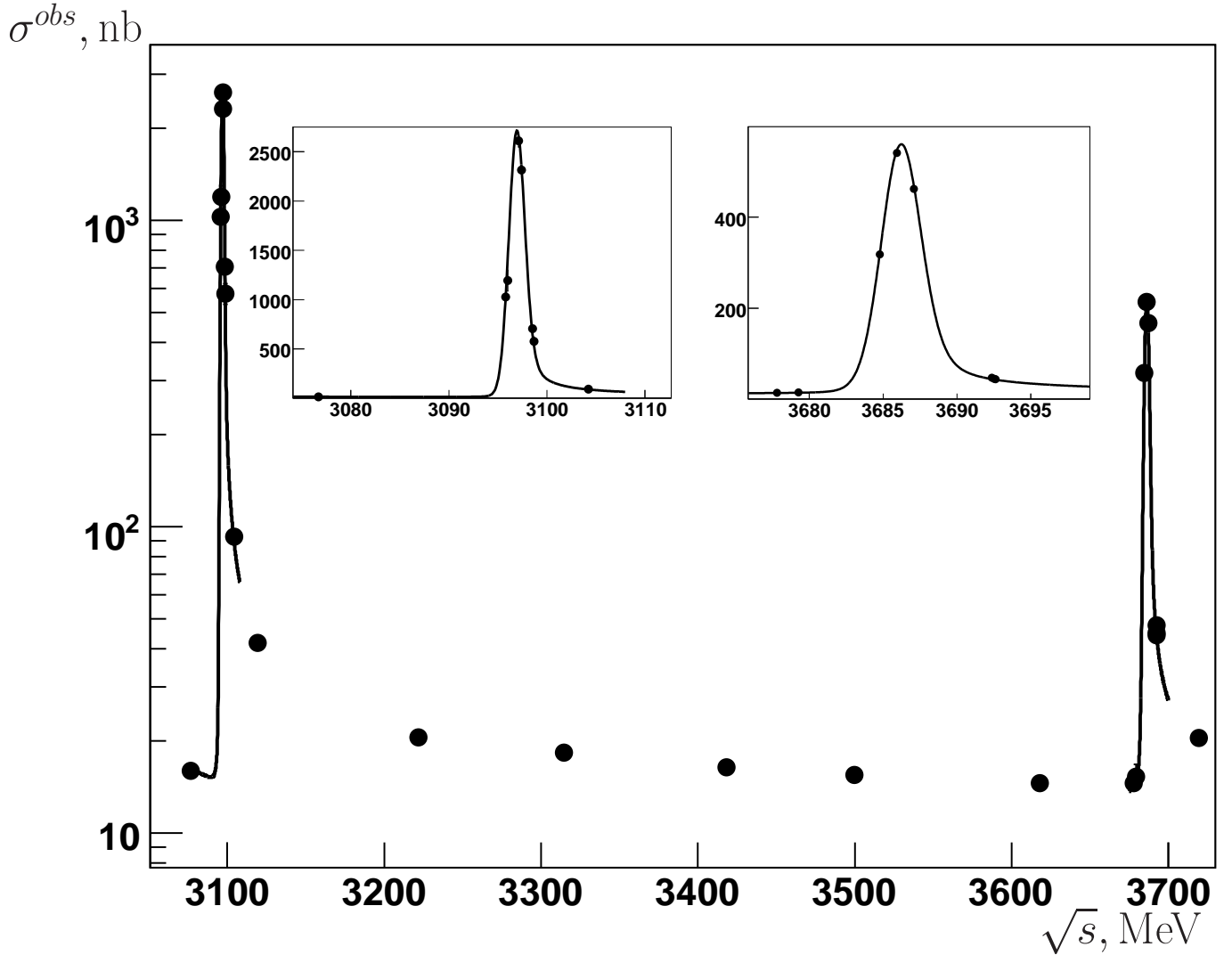


Figure 1: The observed multihadronic cross section as a function of the c.m. energy for the two scans. The curves are the result of the fits of the narrow resonances. The insets show closeup of the J/ψ and $\psi(2S)$ regions.

The radiative correction factor is determined by excluding a contribution of the J/ψ and $\psi(2S)$ resonances and can be written as

$$1+\delta(s) = \int \frac{dx}{1-x} \frac{\mathcal{F}(s,x)}{|1 - \tilde{\Pi}((1-x)s)|^2} \frac{\tilde{R}((1-x)s) \varepsilon((1-x)s)}{R(s) \varepsilon(s)}, \quad (3)$$

where $\mathcal{F}(s,x)$ is the radiative correction kernel [26]. The variable x is a fraction of s lost due to the initial-state radiation. The vacuum polarization operator $\tilde{\Pi}$ and the quantity \tilde{R} do not include a contribution of narrow resonances, details of the calculation are presented in Sec. 4.7.

In the approach described above we extract the R_{uds} value. By adding the contribution of narrow resonances we obtain the quantity R .

4.2. Monte Carlo simulation

The KEDR simulation program is based on the GEANT package, version 3.21 [27].

To simulate single-photon annihilation to hadrons we employ the JETSET 7.4 code [28] with the parameters tuned at each energy point. As an alternative way of generating events of the uds continuum we use the LUARLW generator [29].

Bhabha scattering events required for the precise luminosity determination are simulated by BHWIDE [30]. The MCGPJ generator [31] provides simulation of $\mu^+\mu^-$ events and the $e^+e^- \rightarrow e^+e^-\gamma$ process as an alternative to BHWIDE. The detection efficiency for $\tau^+\tau^-$ events was obtained using the KORALB event generator [32]. The two-photon processes $e^+e^- \rightarrow e^+e^-X$ are simulated with the generators described in Refs. [35, 36, 37].

The J/ψ and $\psi(2S)$ decays were simulated with the tuned version of the BES generator [33] based on the JETSET 7.4 code [24, 38].

During the all experiment random trigger events were recorded. These events were embedded into the Monte Carlo simulated data to account for various detector noises and a coincidence of the simulated processes with the accelerator and cosmic back-

Table 3: Relative contribution of the J/ψ and $\psi(2S)$ resonances to the observed multihadronic cross section. Negative signs correspond to resonance – continuum interference.

Point	$\frac{\sigma_{J/\psi}}{\sigma_{\text{obs}}}, \%$	$\frac{\sigma_{\psi(2S)}}{\sigma_{\text{obs}}}, \%$
1	-7.24(interference)	
2	59.71	
3	22.63	
4	14.83	
5	10.75	
6	8.76	
7	6.80	-0.76(interference)
8	4.05	28.27

grounds.

The most important event characteristics are presented in Fig. 2, from which one can see that the experimental and simulated distributions agree rather well.

4.3. Event selection and detection efficiencies

In the offline analysis both experimental and simulated events pass the software event filter. By using a digitized response of the detector subsystems the software filter recalculates the PT and ST decisions with stringent conditions. This procedure reduces a systematic uncertainty due to trigger instabilities and uncertainties on the hardware thresholds.

To suppress the machine background to an acceptable level, the following PT conditions were used by OR:

- signals from \geq two non-adjacent scintillation counters ,
- signal from the LKr calorimeter ,
- coincidence of the signals from two CsI endcaps.

Signals from two particles with the angular separation $\gtrsim 20^\circ$ should satisfy numerous ST conditions.

The MC simulation shows that the trigger efficiency for continuum uds production increase from 96.2% at 3.08 GeV to 98.0% at 3.72 GeV.

Selection criteria for multihadronic events are presented in Table 4 and their description is given below. Here $N_{\text{track}}^{\text{IP}}$ is the number of tracks originated from the interaction region defined as: $\rho < 5$ mm, $|z_0| < 130$ mm, where ρ is the track impact parameter relative to the beam axis and z_0 – the coordinate of the closest approach point. The $\tilde{N}_{\text{track}}^{\text{IP}}$ is the number of tracks satisfying the conditions above with E/p less than 0.6, where E/p means the ratio of the energy deposited in the calorimeter to the measured momentum of the charged particle. The multiplicity $N_{\text{particles}}$ is a sum of the number of charged tracks and the number of neutral particles detected in the calorimeters.

The observable energy E_{obs} is defined as a sum of the photon energies measured in the electromagnetic calorimeter and charged particle energies computed from the track momenta

Table 4: Selection criteria for hadronic events which were used by AND.

Variable	Allowed range
$N_{\text{particles}} \geq 3$ OR $\tilde{N}_{\text{track}}^{\text{IP}} \geq 2$	
$N_{\text{track}}^{\text{IP}}$	≥ 1
E_{obs}	> 1.6 GeV
$E_{\gamma}^{\text{max}}/E_{\text{beam}}$	< 0.82
E_{cal}	> 0.65 GeV
H_2/H_0	< 0.9
$ P_z^{\text{miss}}/E_{\text{obs}} $	< 0.6
$E_{\text{LKr}}/E_{\text{cal}}$	> 0.15
$ Z_{\text{vertex}} $	< 15.0 cm

Table 5: Detection efficiency for the uds continuum in % (statistical errors only).

Point	$\mathcal{E}_{\text{JETSET}}$	$\mathcal{E}_{\text{LUARLW}}$	$\delta\mathcal{E}/\mathcal{E}$
1	76.91 ± 0.13	76.77 ± 0.13	-0.2 ± 0.2
2	76.77 ± 0.13	76.95 ± 0.13	$+0.2 \pm 0.2$
3	77.09 ± 0.13	76.96 ± 0.13	-0.2 ± 0.2
4	79.22 ± 0.13	80.11 ± 0.13	-1.1 ± 0.2
5	80.38 ± 0.13	80.34 ± 0.13	-0.0 ± 0.2
6	80.47 ± 0.13	79.98 ± 0.13	-0.6 ± 0.2
7	80.56 ± 0.13	80.73 ± 0.13	$+0.2 \pm 0.2$
8	84.03 ± 0.12	83.84 ± 0.12	-0.2 ± 0.2

assuming pion masses. The observable energy cut and limitation on the ratio of the energy of the most energetic photon to the beam energy $E_{\gamma}^{\text{max}}/E_{\text{beam}}$ suppress hadronic events produced via initial-state radiation and thus reduce the uncertainty of radiative corrections. The total calorimeter energy E_{cal} is defined as a sum of the energies of all clusters in the electromagnetic calorimeter. The requirement on it suppresses background from cosmic rays whereas the condition on the ratio of the Fox-Wolfram moments H_2/H_0 [39] is efficient for suppression of the $e^+e^- \rightarrow l^+l^-(\gamma)$ ($l = e, \mu, \tau$) background, that of cosmic rays and some kinds of the machine background. The background from two-photon and beam-gas events is suppressed by the requirement on the ratio $|P_z^{\text{miss}}/E_{\text{obs}}|$, where P_z^{miss} is the z component of the missing momentum. The background from beam-gas events was also suppressed by the condition on the ratio $E_{\text{LKr}}/E_{\text{cal}}$ of the energy deposited in the LKr calorimeter and total calorimeter energy. The event vertex position Z_{vertex} is the average of the z_0 's of the charged tracks. The condition on $|Z_{\text{vertex}}|$ suppresses the background due to beam-gas, beam-wall and cosmic rays.

In addition, the cosmic background is suppressed with the time-of-flight condition and the muon system veto in the cases when more than two tracks did not cross the interaction region.

By applying the selection criteria for hadronic events described above we determined the detection efficiencies for eight

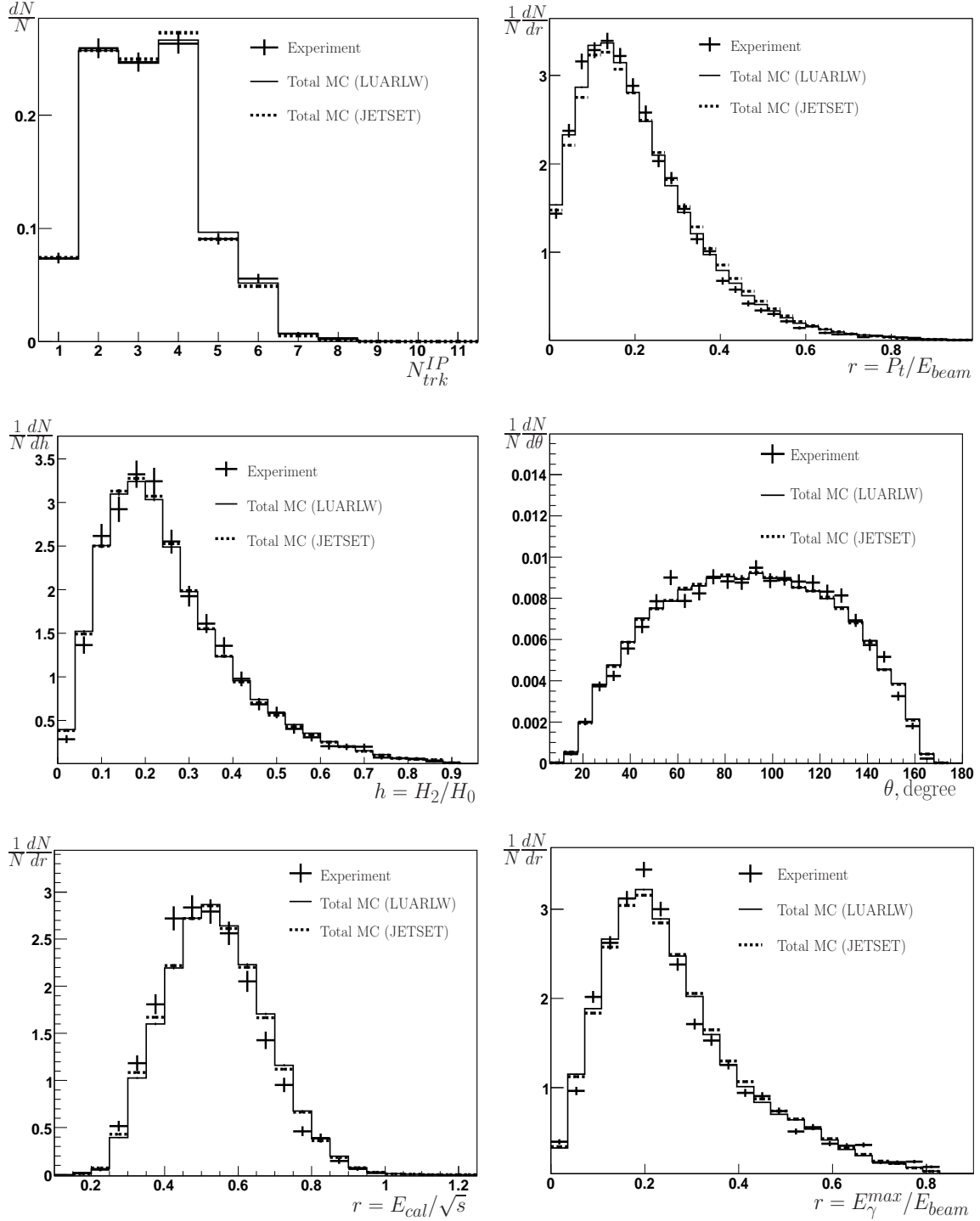


Figure 2: Properties of hadronic events produced in the uds continuum at 3.119 GeV. Here N is the number of events, N_{trk}^{IP} is the number of tracks originated from the interaction region, P_t is a transverse momentum of the track, H_2 and H_0 are Fox-Wolfram moments [39], θ is a polar angle of the track, E_{cal} is energy deposited in the calorimeter, E_{γ}^{max} is energy of the most energetic photon. The experimental distribution and two variants of MC simulation based on LUARLW and JETSET are plotted. Total MC includes simulation of the uds continuum, contributions of the narrow resonances and leptonic channels, we also added the contribution of residual machine background obtained from experimental runs with separated electron and positron beams. The P_t and polar angle distributions include all tracks in the events. The error bars represent statistical errors only. All distributions are normalized to unity.

data points at which the quantity R_{uds} was measured. These values were obtained by using two versions of event simulation and are listed in Table 5. The detection efficiency at point 8 increased drastically mainly due to repairing a quite a few

calorimeter channels.

4.4. Luminosity determination

The integrated luminosity at each point was determined by using Bhabha events detected in the LKr calorimeter in the polar angle range $44^\circ < \theta < 136^\circ$. The criteria for e^+e^- event selection are listed below:

- two clusters, each with the energy above 20% of the beam energy;
- acollinearities of the polar $\delta\theta$ and azimuthal $\delta\phi$ angles are less than 18° ;
- the total energy of these two clusters exceeds the single beam energy;
- the calorimeter energy not associated with these two clusters does not exceed 20% of the total;
- the ratio of the Fox-Wolfram moments $H_2/H_0 > 0.6$.

To reject the background from $e^+e^- \rightarrow \gamma\gamma$, $e^+e^- \rightarrow e^+e^-e^+e^-$ and $e^+e^- \rightarrow \text{hadrons}$ at least one but not more than three tracks originating from the interaction region were required.

4.5. Background processes

To determine the R_{uds} values, we took into account the lepton pair production from the QED processes $e^+e^- \rightarrow e^+e^-$, $e^+e^- \rightarrow \mu^+\mu^-$ and $e^+e^- \rightarrow \tau^+\tau^-$ which are summarized in Table 6.

The contributions of two-photon interactions were studied based on the simulation of $e^+e^- \rightarrow e^+e^-X$ events. We found that the contribution of two-photon events to the continuum cross section grows from 0.47% at 3.077 GeV to 0.51% at 3.72 GeV. The estimated uncertainty in the R_{uds} value due to this contribution is less than 0.2%.

Table 6: The contribution of the lepton pair production to the observed cross section in %.

Point	Process		
	e^+e^-	$\mu^+\mu^-$	$\tau^+\tau^-$
1	5.06 ± 0.24	1.29 ± 0.27	
2	1.67 ± 0.09	0.42 ± 0.12	
3	3.34 ± 0.17	0.72 ± 0.19	
4	4.03 ± 0.19	0.72 ± 0.15	
5	4.01 ± 0.20	0.69 ± 0.16	
6	3.42 ± 0.19	0.49 ± 0.16	
7	4.14 ± 0.21	0.53 ± 0.15	3.37 ± 0.17
8	2.34 ± 0.13	0.33 ± 0.11	4.05 ± 0.20

4.6. Correction to residual machine background

Our estimates of the contributions of the residual machine background to the observed hadronic cross section for different energy points are listed in the column marked "Method 1" in Table 7. These values were obtained by using runs with separated e^+ and e^- bunches, which were recorded at each energy point.

The number of events which passed selection criteria in the background runs was used to evaluate the residual background under the assumption that the background rate is proportional to the beam current and the measured vacuum pressure.

As a cross check, we assumed that the background rate is proportional to the current only. The results are presented in the last column of Table 7, which is marked as "Method 2". The maximal difference of 0.28% between the numbers of background events obtained with these two alternatives was considered as an estimate of the systematic uncertainty.

Table 7: The residual machine background in % of the observed cross section

Point	Background in % (statistical errors only).	
	Method 1	Method 2
1	1.35 ± 0.27	1.29 ± 0.27
2	0.65 ± 0.14	0.80 ± 0.15
3	0.81 ± 0.20	0.86 ± 0.21
4	3.80 ± 0.35	4.08 ± 0.36
5	2.33 ± 0.30	2.19 ± 0.29
6	1.09 ± 0.23	1.15 ± 0.24
7	0.75 ± 0.17	0.76 ± 0.18
8	1.82 ± 0.25	1.94 ± 0.26

4.7. Radiative correction

Numerical calculation of the radiative correction factor was performed according to Eq. (3) by using the compilation of the vacuum polarization data by the CMD-2 group [40] and the relation between $R(s)$ and the hadronic part of the vacuum polarization $\Pi_{\text{hadr}}(s)$:

$$R(s) = -\frac{3}{\alpha} \text{Im} \Pi_{\text{hadr}}(s). \quad (4)$$

To obtain the quantity \tilde{R} and the operator $\tilde{\Pi}$ for Eq. (3) the contribution of the J/ψ and $\psi(2S)$ was subtracted analytically from the vacuum polarization data.

The uds continuum below 3.077 GeV was simulated with the LUARLW generator, that allows us to determine the detection efficiency versus the energy radiated in the initial state.

The x dependence of the detection efficiency is shown in Fig. 3.

The radiative correction factors at different center-of-mass energies are listed in Table 8, while the presented systematic uncertainties will be discussed in more detail in Sec. 5.3.

4.8. J/ψ and $\psi(2S)$ contributions

To determine contributions of narrow resonances to the observed cross section we applied resonance parameters retrieved from the fits. The values presented in Table 2 were corrected for the presence of ISR photons. The corrections were obtained via simulation of J/ψ and $\psi(2S)$ hadron decays at each energy point.

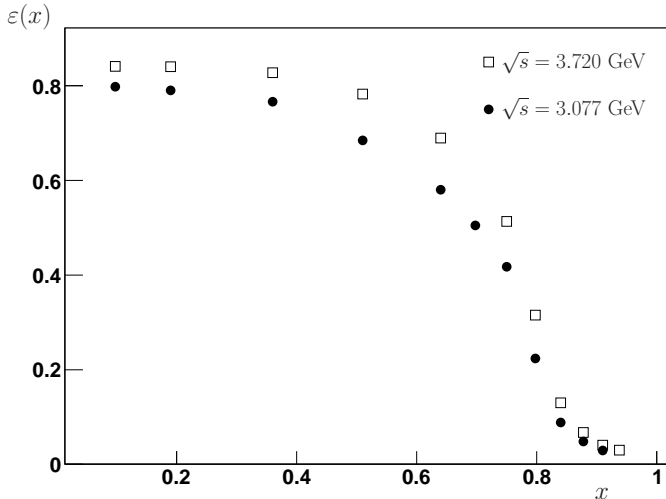


Figure 3: Hadronic detection efficiency versus variable x of Eq. (3) at 3.077 GeV and 3.72 GeV.

Table 8: Radiative correction factor $1 + \delta$.

Point	$1 + \delta$
1	1.1091 ± 0.0089
2	1.1108 ± 0.0089
3	1.1120 ± 0.0056
4	1.1130 ± 0.0078
5	1.1133 ± 0.0067
6	1.1151 ± 0.0056
7	1.1139 ± 0.0078
8	1.1137 ± 0.0056

The detection efficiencies obtained from simulation of hadronic decays in vicinity of narrow resonances are $(79.00 \pm 0.06)\%$ and $(81.40 \pm 0.08)\%$ for J/ψ and $\psi(2S)$, respectively. For both resonances the detection efficiencies obtained by simulation agree with the fit results within the estimated errors.

4.9. Results of energy scan

The results of the R_{uds} measurement obtained in the energy scan are presented in Table 9.

5. Systematic uncertainties and results

5.1. Systematic uncertainty of absolute luminosity determination

The dominant contributions to the systematic error of the absolute luminosity determination with the LKr calorimeter are presented in Table 10.

The uncertainty of the theoretical Bhabha cross section was evaluated comparing the results obtained with the BHWIDE [30] and MCGPJ [31] event generators for all energy points. The maximum difference did not exceed 0.4% and agreed with the accuracy quoted by the authors.

Table 9: Resulting R_{uds} values with their statistical errors.

Point	R_{uds}
1	2.188 ± 0.056
2	2.211 ± 0.046
3	2.214 ± 0.055
4	2.233 ± 0.044
5	2.197 ± 0.047
6	2.224 ± 0.054
7	2.220 ± 0.049
8	2.213 ± 0.047

Table 10: Systematic uncertainties of the luminosity determination.

Source	Uncertainty, %
Cross section calculation	0.4
Calorimeter response	0.4
Calorimeter alignment	0.2
Polar angle resolution	0.1
Background	0.1
MC statistics	0.1
Variation of cuts	0.7
Sum in quadrature	0.9

The systematic uncertainty related to the imperfect simulation of the calorimeter response is about 0.4%. It was quantified by variation of relevant simulation parameters such as the accuracy of the electronic channel calibration, the geometrical factor controlling sensitivity to the energy loss fluctuations between calorimeter electrodes, etc.

The alignment of the tracking system and LKr calorimeter is obtained by reconstructing cosmic rays. By using the primary-vertex distribution of multihadronic and Bhabha events we determined the interaction point position and direction of the beam line. The luminosity uncertainty due to inaccuracy of the alignment is about 0.2%.

The uncertainty related to the difference of the polar angle resolution in simulation and data is less than 0.1%. This uncertainty occurs from the difference in the polar angle resolution observed in experiment and predicted by simulation, because events migrate into or out of the fiducial volume.

The background to Bhabha events from the processes $e^+e^- \rightarrow \mu\mu(\gamma)$ and $e^+e^- \rightarrow \gamma\gamma$ and J/ψ and $\psi(2S)$ decays contributes less than 0.2% to the observed e^+e^- cross section at eight energy points listed in Table 1. It was estimated using MC simulation. At the complementary points of the scan serving for the determination of the J/ψ and $\psi(2S)$ parameters the contributions of the resonance decays to e^+e^- were calculated by the fitting.

The luminosity uncertainty due to the residual machine background does not exceed 0.1%.

In addition, we varied requirements within the fiducial region to evaluate the effect of other possible sources of a systematic uncertainty. The conditions on the polar angle were varied in a range much larger than the angular resolution, the variation in the Bhabha event count reaches 50%. The requirement on the deposited energy was varied in the range of 70 – 90% of the c.m. energy. The sum in quadrature of all errors obtained by variation of the selection criteria is about 0.7% and gives an additional estimate of the systematic uncertainty. Despite possible double counting we add this error to the total luminosity uncertainty to obtain a conservative error estimate.

5.2. Uncertainty due to imperfect simulation of continuum

The systematic uncertainty in the R_{uds} value associated with imperfect simulation of the uds continuum was evaluated by using two different MC simulation models. We considered the detection efficiencies for eight energy points reported in Table 5 obtained with the JETSET and LUARLW hadronic generators. It does not exceed a value of 1.1% which was taken as the systematic uncertainty related to the detection efficiency. This estimate is consistent with our previous result of 1.3% obtained in Ref. [15] and agrees with a value of 0.6% found by the variation of selection criteria in Sec. 5.4

5.3. Systematic uncertainty of the radiative correction

The major sources of systematic uncertainty in the radiative correction factor at each energy point are presented in Table 11.

To evaluate the uncertainty related to a choice of the vacuum polarization operator, two alternatives are compared. The first one was taken from the CMD-2 work [40], the second was obtained from the BES event generator [33]. The difference in the results obtained according to the data of the used variants reaches 0.8% at the points closest to J/ψ and varied from 0.1% to 0.5% at the other points.

The contribution denoted as $\delta R_{uds}(s)$ is associated with the $R_{uds}(s)$ uncertainty. It is less than 0.2% for the entire energy range. The contribution $\delta\epsilon(s)$ of about 0.4% is related to the uncertainty in the $\epsilon(s)$ dependence. A calculation of the radiative corrections according to Eq. (3) requires the interpolation of the detection efficiency presented in Fig. 3 as a function of x . The contribution δ_{calc} is related to the interpolation uncertainty. It was estimated by comparing the results obtained using the linear interpolation and the quadratic one.

5.4. Detector-related uncertainties in R_{uds}

The track reconstruction efficiency was studied by using Bhabha events and low-momentum cosmic tracks and the appropriate correction was introduced in the MC simulation. The uncertainty of the correction introduces an additional systematic uncertainty of about 0.2%. We also used two methods to achieve data and MC consistency in the momentum and angular resolution. The first way was to scale the spatial resolution of the drift chamber, while in the second method assumed scaling systematic uncertainties of the calibration parameters of the tracking system. The maximal obtained variation of the detection efficiency at various energies is less than 0.3%. Thus, the uncertainty related to track reconstruction is about 0.4%.

Table 11: Systematic uncertainties of the radiative correction.

Point	Uncertainty, %				
	Contributions				Total
	Π approx.	$\delta R_{uds}(s)$	$\delta\epsilon(s)$	δ_{calc}	
1	0.7	0.2	0.4	0.1	0.8
2	0.7	0.1	0.4	0.1	0.8
3	0.2	0.1	0.4	0.1	0.5
4	0.5	0.1	0.4	0.1	0.7
5	0.4	0.1	0.4	0.1	0.6
6	0.2	0.1	0.4	0.1	0.5
7	0.5	0.1	0.4	0.1	0.7
8	0.1	0.2	0.4	0.1	0.5

The trigger efficiency uncertainty is about 0.2% and mainly comes from the calorimeter thresholds in the secondary trigger. It was estimated by varying the threshold in the software event filter.

The trigger and event selection efficiency depend on the calorimeter response to hadrons. We estimated the uncertainty of 0.2% related to the simulation of nuclear interaction by comparing the efficiencies obtained with the packages GHEISHA [41] and FLUKA [42] which are implemented in GEANT 3.21 [27].

The effect of other possible sources of the detector-related uncertainty was evaluated by varying the event selection criteria that are presented in Table 12. Tightening of some requirements listed in Table 12 by several times varies a contribution to the observed cross section of physical and machine background events and significantly changes the detection efficiency. That allows us to verify uncertainties associated with the background and radiative corrections.

All observed R_{uds} variations were smaller than their statistical errors and can originate from the already considered sources of uncertainties or the statistical fluctuations. By keeping a conservative estimate, we added them in the total uncertainty.

Table 12: R_{uds} uncertainty due to variation of the selection criteria for hadronic events.

Condition/Variable	Range variation	R_{uds} variation in %
$N_{\text{particles}} \geq 3$ OR $\tilde{N}_{\text{track}}^{\text{IP}} \geq 2$	$N_{\text{particles}} \geq 4$ OR $\tilde{N}_{\text{track}}^{\text{IP}} \geq 2$	0.1
$N_{\text{track}}^{\text{IP}}$	≥ 1 OR no cut	0.1
E_{obs}	$> 1.4 \div 1.8$ GeV	0.3
$E_{\gamma}^{\text{max}}/E_{\text{beam}}$	$< 0.6 \div 0.9$	0.3
E_{cal}	$> 0.5 \div 0.75$ GeV	0.2
H_2/H_0	$< 0.7 \div 0.93$	0.2
$ P_z^{\text{miss}}/E_{\text{obs}} $	$< 0.6 \div 0.8$	0.2
$E_{\text{LKr}}/E_{\text{cal}}$	$> 0.15 \div 0.25$	0.1
$ Z_{\text{vertex}} $	$< 20.0 \div 13.0$ cm	0.2
Sum in quadrature		0.6

5.5. Summary of systematic uncertainties and results

The major sources of the systematic uncertainty on the R_{uds} value are listed in Table 13.

Table 13: R_{uds} systematic uncertainties in % assigned to each energy point.

	1	2	3	4	5	6	7	8
Luminosity	0.9	0.9	0.9	0.9	0.9	0.9	0.9	0.9
Radiative correction	0.8	0.8	0.5	0.7	0.6	0.5	0.7	0.5
Continuum simulation	1.1	1.1	1.1	1.1	1.1	1.1	1.1	1.1
Track reconstruction	0.4	0.4	0.4	0.4	0.4	0.4	0.4	0.4
e^+e^-X contribution	0.2	0.2	0.2	0.2	0.2	0.2	0.2	0.2
l^+l^- contribution	0.4	0.4	0.4	0.3	0.3	0.3	0.4	0.4
Trigger efficiency	0.2	0.2	0.2	0.2	0.2	0.2	0.2	0.2
Nuclear interaction	0.2	0.2	0.2	0.2	0.2	0.2	0.2	0.2
Cuts variation	0.6	0.6	0.6	0.6	0.6	0.6	0.6	0.6
J/ψ and $\psi(2S)$	0.1	1.8	0.4	0.2	0.1	0.1	0.1	1.1
Machine background	0.4	0.8	0.5	0.6	0.5	0.4	0.4	0.6
Sum in quadrature	1.9	2.7	1.9	1.9	1.8	1.8	1.9	2.2

During data collection at a given energy point the relative beam energy variation was less than 10^{-3} allowing us to neglect this source of uncertainty.

The results obtained at most points supplement the data published in Ref. [15]. In order to use these data in the calculations of the dispersion integrals it is important to combine results from both experiments taking correlated uncertainties properly into account. This requires to determine the common components of the uncertainties which are the same for each experiment. The corresponding contributions to the systematic uncertainty are listed in Table 14.

The results of the two scans were averaged using their statistical uncertainties and the uncorrelated parts of the systematic ones. The formal description of the averaging procedure can be found in Ref. [24]. The obtained R_{uds} and R values as well as luminosity-weighted average center-of-mass energies are presented in Table 15. As mentioned above, the contribution of narrow resonances to $R(s)$ is not negligible in the resonance region. This contribution was determined analytically by using "bare" parameters of the resonances, which were calculated based on the PDG data [25].

The inaccuracy of R associated with the resonance parameters is negligible in comparison with the other uncertainties, so the errors for the values of R and R_{uds} are the same.

6. Summary

By combining new data with our previous results we determined the values of R_{uds} and R at nine center-of-mass energy points between 3.08 and 3.72 GeV. The total accuracy is about or better than 2.6% at most of energy points with a systematic

Table 14: Correlated systematic uncertainties R_{uds} in % for data of 2011 and 2014.

Source	Uncertainty in %
Luminosity	
Cross section calculation	0.4
Radiative correction	
Π approx.	$0.1 \div 0.3$
$\delta R_{\text{uds}}(s)$	$0.1 \div 0.2$
$\delta \varepsilon(s)$	0.2
Continuum simulation	
e^+e^-X contribution	0.1
l^+l^- contribution	0.2
Trigger efficiency	0.2
Nuclear interaction	0.2
Sum in quadrature	1.3

uncertainty of about 1.9%. This result provides the most precise information about R in this energy range. The measured R values are shown in Fig. 4.

The weighted average $\bar{R}_{\text{uds}} = 2.204 \pm 0.013 \pm 0.030$ is approximately one sigma higher than that theoretically expected, $R_{\text{uds}}^{\text{pQCD}} = 2.16 \pm 0.01$ calculated according to the pQCD expansion [43] for $\alpha_s(m_\tau) = 0.333 \pm 0.013$ obtained from semi-leptonic τ decays [44].

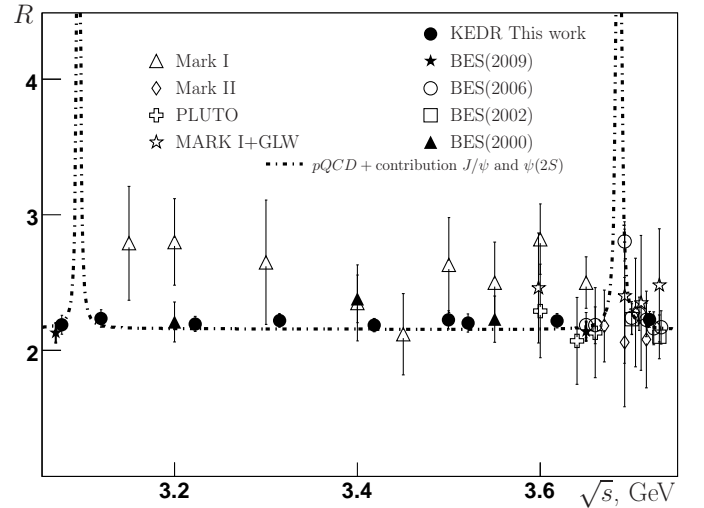


Figure 4: The quantity R versus the c.m. energy and the sum of the prediction of perturbative QCD and a contribution of narrow resonances.

It should be noted that while calculating the dispersion integrals in this energy range it is preferable to use the measured $R_{\text{uds}}(s)$ values adding the contribution of narrow resonances cal-

Table 15: Measured values of $R_{uds}(s)$ and $R(s)$ with statistical and systematic uncertainties.

Data 2011 [15]		Data 2014		Combination	
\sqrt{s} , MeV	$R_{uds}(s)$	\sqrt{s} , MeV	$R_{uds}(s)$	\sqrt{s} , MeV	$R_{uds}(s)\{R(s)\}$
-	-	3076.7 ± 0.2	$2.188 \pm 0.056 \pm 0.042$	3076.7 ± 0.2	$2.188 \pm 0.056 \pm 0.042$
3119.9 ± 0.2	$2.215 \pm 0.089 \pm 0.066$	3119.2 ± 0.2	$2.211 \pm 0.046 \pm 0.060$	3119.6 ± 0.4	$2.212\{2.235\} \pm 0.042 \pm 0.050$
3223.0 ± 0.6	$2.172 \pm 0.057 \pm 0.045$	3221.8 ± 0.2	$2.214 \pm 0.055 \pm 0.042$	3222.5 ± 0.8	$2.194\{2.195\} \pm 0.040 \pm 0.037$
3314.7 ± 0.7	$2.200 \pm 0.056 \pm 0.043$	3314.7 ± 0.4	$2.233 \pm 0.044 \pm 0.042$	3314.7 ± 0.6	$2.220\{2.220\} \pm 0.035 \pm 0.036$
3418.2 ± 0.2	$2.168 \pm 0.050 \pm 0.042$	3418.3 ± 0.4	$2.197 \pm 0.047 \pm 0.040$	3418.3 ± 0.3	$2.186\{2.186\} \pm 0.032 \pm 0.036$
-	-	3499.6 ± 0.4	$2.224 \pm 0.054 \pm 0.040$	3499.6 ± 0.4	$2.224\{2.224\} \pm 0.054 \pm 0.040$
3520.8 ± 0.4	$2.200 \pm 0.050 \pm 0.044$	-	-	3520.8 ± 0.4	$2.200\{2.201\} \pm 0.050 \pm 0.044$
3618.2 ± 1.0	$2.201 \pm 0.059 \pm 0.044$	3618.1 ± 0.4	$2.220 \pm 0.049 \pm 0.042$	3618.2 ± 0.7	$2.212\{2.218\} \pm 0.038 \pm 0.037$
3719.4 ± 0.7	$2.187 \pm 0.068 \pm 0.060$	3719.6 ± 0.2	$2.213 \pm 0.047 \pm 0.049$	3719.5 ± 0.5	$2.204\{2.228\} \pm 0.039 \pm 0.043$

culated analytically. This approach prevents a possible double counting.

Acknowledgments

We greatly appreciate the efforts of the staff of VEPP-4M to provide good operation of the complex during long term experiments. The authors are grateful to V. P. Druzhinin for useful discussions. The Siberian Branch of the Russian Academy of Sciences Siberian Supercomputer Center and Novosibirsk State University Supercomputer Center are gratefully acknowledged for providing supercomputer facilities.

This work has been supported by Russian Science Foundation (project N 14-50-00080).

7. Appendix

At present, KEDR measured the R values at twenty two center-of-mass energies between 1.84 and 3.72 GeV listed in Table 16.

To use $R(s)$ data it is necessary to take into account point-by-point correlated effects. The analysis of the sources of systematic uncertainties makes it possible to identify common contributions in the listed data sets. Similarly to the Table 14 presented above, the correlated systematic uncertainties R_{uds} for other data sets are listed in Table 17. In keeping with a conservative approach, we believe these contributions are completely correlated, that allows us to write down an approximate covariance matrix for systematic uncertainties (Table 18). Note that statistical errors in our R results are fully uncorrelated.

References

- [1] M. Davier *et al.*, Eur. Phys. J. C **71**, 1515 (2011).
- [2] K. Hagiwara *et al.*, J. Phys. J. G **38**, 085003 (2011).
- [3] N. Brambilla *et al.*, Eur. Phys. J. C **71**, 1534 (2011).
- [4] M. Grilli *et al.*, Nuovo Cim. Lett. A **13**, 593 (1973).
- [5] P. A. Rapidis *et al.*, Phys. Rev. Lett. **39**, 526 (1977).
- [6] J. Burmester *et al.*, Phys. Lett. B **66**, 395 (1977).

Table 16: Summary table of KEDR results. Actual energies and measured R values.

Point	Energy	$R_{uds}(s)\{R(s)\}$
Data 2010 [16]		
1	1841.0 ± 2	$2.226 \pm 0.139 \pm 0.158$
2	1937.0 ± 2	$2.141 \pm 0.081 \pm 0.073$
3	2037.3 ± 2	$2.238 \pm 0.068 \pm 0.072$
4	2135.7 ± 2	$2.275 \pm 0.072 \pm 0.055$
5	2239.2 ± 2	$2.208 \pm 0.069 \pm 0.053$
6	2339.5 ± 2	$2.194 \pm 0.064 \pm 0.048$
7	2444.1 ± 2	$2.175 \pm 0.067 \pm 0.048$
8	2542.6 ± 2	$2.222 \pm 0.070 \pm 0.047$
9	2644.8 ± 2	$2.220 \pm 0.069 \pm 0.049$
10	2744.6 ± 2	$2.269 \pm 0.065 \pm 0.050$
11	2849.7 ± 2	$2.223 \pm 0.065 \pm 0.047$
12	2948.9 ± 2	$2.234 \pm 0.064 \pm 0.051$
13	3048.1 ± 2	$2.278 \pm 0.075 \pm 0.048$
Combined Data 2011 [15] and 2014 (This work)		
14	3076.7 ± 0.2	$2.188 \pm 0.056 \pm 0.042$
15	3119.6 ± 0.4	$2.212\{2.235\} \pm 0.042 \pm 0.050$
16	3222.5 ± 0.8	$2.194\{2.195\} \pm 0.040 \pm 0.037$
17	3314.7 ± 0.6	$2.220\{2.220\} \pm 0.035 \pm 0.036$
18	3418.3 ± 0.3	$2.186\{2.186\} \pm 0.032 \pm 0.036$
19	3499.6 ± 0.4	$2.224\{2.224\} \pm 0.054 \pm 0.040$
20	3520.8 ± 0.4	$2.200\{2.201\} \pm 0.050 \pm 0.044$
21	3618.2 ± 1.0	$2.212\{2.218\} \pm 0.038 \pm 0.037$
22	3719.4 ± 0.7	$2.204\{2.228\} \pm 0.039 \pm 0.043$

- [7] C. Bacci *et al.*, Phys. Lett. B **86**, 234(1979).
- [8] R. H. Schindler *et al.*, Phys. Rev. D **21**, 2716 (1980).
- [9] B. Esposito *et al.*, Nuovo Cim. Lett. **30**, 65 (1981).
- [10] J. L. Siegrist *et al.*, Phys. Lett. B **26**, 969 (1982).

Table 17: Correlated systematic uncertainties of R_{uds} in % for data of 2010, 2011 and 2014.

Source	Uncertainty in %	
	Data 2010	Data 2010 / Data 2011, 2014
Luminosity		
Cross section calc.	0.5	0.4
Calorimeter response	0.7	-
Calorimeter alignment	0.2	0.2
Radiative correction		
Π approx.	0.3	0.1
$\delta R_{uds}(s)$	0.2	0.2
$\delta \varepsilon(s)$	0.3	0.2
Continuum simulation	1.2	1.1
Track reconstruction	0.5	0.4
e^+e^-X contribution	0.2	0.1
l^+l^- contribution	0.3	0.2
Trigger efficiency	0.3	0.2
Nuclear interaction	0.4	0.2
Sum in quadrature	1.8	1.3

[11] J. Z. Bai *et al.* (BES Collaboration), Phys. Rev. Lett. **84**, 594 (2000).
[12] J. Z. Bai *et al.* (BES Collaboration), Phys.Rev.Lett. **88**, 101802 (2002).
[13] M. Ablikim *et al.* (BES Collaboration), Phys. Rev. Lett. **97**, 262001 (2006).
[14] M. Ablikim *et al.* (BES Collaboration), Phys. Lett. B **677**, 239 (2009).
[15] V.V. Anashin *et al.* (KEDR Collaboration), Phys. Lett. B **753**, 533 (2016).
[16] V.V. Anashin *et al.* (KEDR Collaboration), Phys. Lett. B **770**, 174 (2017).
[17] V. V. Anashin *et al.*, Stockholm 1998, EPAC 98*, 400 (1998).
[18] A. D. Bukin *et al.*, Absolute Calibration of Beam Energy in the Storage Ring. Phi-Meson Mass Measurement, Preprint IYF-75-64, 1975.
[19] A. N. Skrinsky and Y. M. Shatunov, Sov. Phys. Usp. **32**, 548 (1989).
[20] V. M. Aulchenko *et al.* (KEDR Collaboration), Phys. Lett. B **573**, 63 (2003).
[21] V. V. Anashin *et al.* (KEDR Collaboration), Phys. Lett. B **749**, 50 (2015).
[22] V. V. Anashin *et al.* (KEDR Collaboration), Phys. of Part. and Nucl. **44**, 657 (2013).
[23] S. E. Baru *et al.*, Instrum. Exp. Tech. **54**, 335 (2011).
[24] V. V. Anashin *et al.* (KEDR Collaboration), Phys. Lett. B **711**, 280 (2012).
[25] K. A. Olive *et al.* (PDG), Chin. Phys. C **38**, 090001 (2014).
[26] E. A. Kuraev and V. S. Fadin, Sov. J. Nucl. Phys. **41**, 466 (1985).
[27] GEANT – Detector Description and Simulation Tool CERN Program Library Long Writeup W5013.
[28] T. Sjostrand, M. Bengtsson, Comp. Phys. Comm. **43**, 367 (1987).
[29] Haiming Hu and An Tai, eConf C010430 (2001) T24, arXiv:hep-ex/0106017.
[30] S. Jadach, W. Placzek, B. F. L. Ward, Phys. Lett. B **390**, 298 (1997).
[31] A. B. Arbuzov *et al.*, Eur. Phys. J. C **46**, 689 (2006).
[32] S. Jadach, Z. Was, Comp. Phys. Comm. **85**, 453 (1995).
[33] J. C. Chen *et al.*, Phys. Rev. D **62**, 034003 (2000).
[34] K. Nakamura *et al.* (PDG), J. Phys. G **37**, 075021 (2010).
[35] F. A. Berends *et al.*, Comp. Phys. Comm. **40**, 285 (1986).
[36] F. A. Berends *et al.*, Comp. Phys. Comm. **40**, 271 (1986).
[37] V. A. Tayursky, S. I. Eidelman, Preprint IYaF 2000-78, Novosibirsk 2000 (in Russian).
[38] V. V. Anashin *et al.* (KEDR Collaboration), JHEP 1805, 119 (2018), arXiv:1801.01958.

[39] G. C. Fox, S. Wolfram, Nucl. Phys. B **149**, 413 (1979).
[40] S. Actis *et al.*, Eur. Phys. J. C **66**, 585 (2010).
[41] H.C. Fesefeldt, Technical Report PITHA-85-02, III Physikalisches Institut, RWTH Aachen Physikzentrum, 5100 Aachen, Germany, Sep. 1985.
[42] A. Fassò *et al.*, Talk at the Computing in High Energy and Nuclear Physics (CHEP03), arXiv:physics/0306162.
[43] P. A. Baikov *et al.*, Phys. Lett. B **714**, 62 (2012).
[44] N. Brambilla *et al.*, Eur. Phys. J. C **74**, 2981 (2014).

Table 18: The correlation matrix for systematic uncertainties of the R values obtained in the KEDR experiments.

Point	Correlation Matrix																					
1	1	0.139	0.143	0.193	0.192	0.212	0.212	0.216	0.207	0.211	0.216	0.201	0.222	0.126	0.106	0.143	0.147	0.147	0.133	0.120	0.143	0.123
2		1	0.309	0.418	0.408	0.445	0.437	0.466	0.446	0.457	0.467	0.434	0.48	0.264	0.227	0.301	0.317	0.307	0.286	0.255	0.306	0.262
3			1	0.423	0.425	0.470	0.470	0.480	0.460	0.463	0.480	0.442	0.486	0.280	0.235	0.318	0.327	0.327	0.294	0.267	0.318	0.273
4				1	0.575	0.635	0.635	0.649	0.622	0.61	0.649	0.598	0.637	0.379	0.318	0.43	0.442	0.442	0.398	0.361	0.430	0.370
5					1	0.621	0.621	0.642	0.615	0.629	0.643	0.598	0.661	0.370	0.312	0.420	0.437	0.432	0.394	0.353	0.422	0.362
6						1	0.677	0.709	0.679	0.695	0.710	0.661	0.730	0.404	0.345	0.458	0.482	0.471	0.435	0.387	0.466	0.398
7							1	0.709	0.679	0.695	0.710	0.661	0.730	0.401	0.345	0.458	0.482	0.467	0.435	0.387	0.466	0.398
8								1	0.695	0.710	0.725	0.675	0.745	0.423	0.355	0.480	0.493	0.493	0.445	0.403	0.480	0.413
9									1	0.681	0.695	0.647	0.715	0.405	0.340	0.459	0.472	0.472	0.426	0.386	0.459	0.395
10										1	0.710	0.654	0.701	0.414	0.348	0.470	0.483	0.483	0.435	0.395	0.470	0.405
11											1	0.675	0.745	0.423	0.355	0.480	0.494	0.494	0.445	0.404	0.480	0.413
12												1	0.687	0.394	0.331	0.447	0.459	0.459	0.413	0.376	0.447	0.385
13													1	0.435	0.365	0.494	0.508	0.508	0.457	0.415	0.494	0.425
14														1	0.394	0.523	0.551	0.535	0.498	0.443	0.532	0.455
15															1	0.447	0.463	0.459	0.418	0.376	0.447	0.385
16																1	0.625	0.611	0.565	0.502	0.604	0.516
17																	1	0.643	0.580	0.526	0.625	0.538
18																		1	0.58	0.516	0.621	0.530
19																			1	0.475	0.565	0.486
20																				1	0.508	0.434
21																					1	0.520
22																						1